Urban Climate 66 (2026) 102796

Contents lists available at ScienceDirect

Urban Climate

journal homepage: www.elsevier.com/locate/uclim

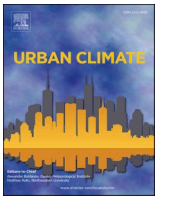

Impacts of urban aerosols and land use on clouds and precipitation in urban and adjacent non-urban areas

Seoung Soo Lee [a,b,c,*], Jinho Choi [d], Kyong-Hwan Seo [d,e], Junshik Um [d,f,g,*], Hyunkyoung Kim [f,g], Chang Hoon Jung [h], Sang-Keun Song [i,*], Manguttathil G. Manoj [j]

[a] Science and Technology Corporation, Hampton, Virginia, USA
[b] Earth System Science Interdisciplinary Center, University of Maryland, College Park, MD, USA
[c] Research Center for Climate Sciences, Pusan National University, Busan, Republic of Korea
[d] Department of Atmospheric Sciences, Pusan National University, Busan, Republic of Korea
[e] Institute for Future Earth, Pusan National University, Busan, Republic of Korea
[f] Institute of Environmental Studies, Pusan National University, Busan, Republic of Korea
[g] BK21 School of Earth and Environmental Systems, Division of Earth Environmental System, Department of Atmospheric Sciences, Pusan National University, Busan, Republic of Korea
[h] Department of Health Management, Kyungin Women's University, Incheon, Republic of Korea
[i] Department of Earth and Marine Sciences, Jeju National University, Jeju, Republic of Korea
[j] Advanced Centre for Atmospheric Radar Research, Cochin University of Science and Technology, Kerala, India

ARTICLE INFO

Keywords:
Urban area
Non-urban area
Aerosol
Land use
Clouds and precipitation

ABSTRACT

This study investigates impacts of urban aerosols and land use on precipitation not only in an urban area but also in an adjacent non-urban area, focusing on a mesoscale convective system in the Seoul metropolitan region, South Korea and using a cloud-system-resolving model. Elevated urban aerosol concentrations in turn elevate concentrations of cloud condensation nuclei, enhancing droplet nucleation and lifting up condensation rates, which intensify updrafts. This leads to increased precipitation in the urban area but reduces very heavy precipitation in the non-urban area by disrupting the moist static energy (MSE) fluxes. Conversely, urban land use weakens the surface latent-heat fluxes, suppressing precipitation in the urban area while enhancing precipitation in the non-urban area also by disrupting the MSE fluxes. These findings underscore the importance of evaluating both urban and adjacent non-urban regions—and of considering the dual roles of aerosols and land-use change—to achieve a comprehensive understanding of how urbanization reshapes regional hydrometeorological processes and precipitation patterns

1. Introduction

Urbanization, which involves high population density and extensive infrastructure development, represents one of the most profound human-induced transformations of the natural environment. It modifies land surfaces, atmospheric dynamic and thermodynamic processes, and energy balances, thereby influencing both local and regional atmospheric and hydrological systems. Despite

* Corresponding authors.
E-mail addresses: slee1247@umd.edu (S.S. Lee), jjunum@pusan.ac.kr (J. Um), songsk@jejunu.ac.kr (S.-K. Song).

https://doi.org/10.1016/j.uclim.2026.102796
Received 23 February 2025; Received in revised form 11 December 2025; Accepted 16 January 2026
Available online 10 March 2026

extensive research on these topics, our understanding of how urbanization alters coupled atmospheric and hydrological processes—particularly clouds and precipitation—remains limited (Climate Change Science Program and Subcommittee on Global Change Research, 2003; Shepherd, 2005; Reale et al., 2011; Bercos-Hickey et al., 2017; Masson et al., 2020; McLeod et al., 2017, 2024). This knowledge gap underscores the need for integrated investigations that consider not only human components but also atmospheric and hydrological processes of the urban–atmosphere system.

The urbanization impacts flooding primarily by replacing permeable soils with impermeable surfaces that lowers the removal efficiency of water pooled on the urban surface (Miller and Hutchins, 2017; Wang et al., 2019; Li et al., 2024). Urban land use is represented by these impermeable surfaces. Urban land use in turn generates the urban heat island (UHI), affecting convective clouds and precipitation patterns in urban areas (Bouvette et al., 1982; Baik et al., 2001; Diem and Brown, 2003; Burian and Shepherd, 2005; Shepherd, 2005; Hidaldo et al., 2010; Chen et al., 2015; McLeod et al., 2017, 2024). UHI raises land surface temperatures (LTs) in urban areas compared to adjacent suburban and rural areas, often collectively termed “non-urban areas”. This LT disparity drives mesoscale circulations across urban and non-urban areas, impacting convective clouds and associated precipitation there (e.g., Shepherd et al., 2002; Hidaldo et al., 2010; Niyogi et al., 2011; Haberlie et al., 2015; Li et al., 2017; Sato et al., 2020).

Another consequence of urbanization is the presence of pollutant aerosols linked to industrial activities and population growth. Previous research has demonstrated that urban aerosols enhance precipitation in urban areas through aerosol-cloud interactions, which involve aerosol impacts on latent-heat processes, and aerosol-radiation interactions, which involve aerosol impacts on radiation (van den Heever and Cotton, 2007; Lee et al., 2018; Fan et al., 2020; Lin et al., 2021). Due to pollutant aerosols, aerosol loading or concentrations tend to be higher in urban areas, compared to non-urban areas (Diem and Brown, 2003; Shepherd, 2005; Shelley et al., 2014; Lee et al., 2018; Casquero-Vera et al., 2022). Modeling and observational studies (e.g., Rotstayn and Lohmann, 2002; Menon et al., 2002; Lau and Kim, 2006; Rotstayn et al., 2007; Bell et al., 2008; Wilcox et al., 2010; Lee, 2012; Lee et al., 2014; Lee et al., 2018; Fan et al., 2020; Leung and van den Heever, 2023) have demonstrated that the spatial inhomogeneity of aerosol concentrations generates circulations that extend over both urban and non-urban areas and influence convective clouds and precipitation there.

To address the urbanization influences on convective clouds and precipitation in a comprehensive way, this study examines how spatial inhomogeneities in LT and aerosol concentrations between urban and non-urban areas modulate convective clouds and precipitation over these areas. For the examination, we focus on an observed mesoscale convective system (MCS) that was from 13:00 local solar time (LST) to 19:00 LST on June 22nd, 2016, in the Seoul metropolitan region of South Korea. Leveraging a high-resolution cloud-system-resolving model (CSRM), we perform numerical simulations to isolate the individual and combined impacts of urban aerosols and land use. Our methodology includes a control run incorporating realistic urban conditions and two primary sensitivity experiments: one with urban aerosol concentrations reduced to non-urban levels and another with an urban land use replaced by a non-urban counterpart. These experiments are designed to test the hypothesis that impacts of urban aerosols and land use on clouds and precipitation go beyond an urban area to a non-urban area by generating and driving mesoscale circulations. Stated differently, through the experiments, this study aims to identify how impacts of urban aerosols and land use operate individually and collaboratively and demonstrate that these impacts have tele-connected influences extending into a surrounding non-urban area. To fulfill the aim, the spatial and temporal evolution of precipitation and associated dynamics, thermodynamic and microphysical variables are compared across the simulations. The fulfillment of the aim will underscore the importance of jointly evaluating urban and non-urban areas, as well as the roles of urban aerosols and land use, to comprehensively understand urbanization's influence on regional hydrometeorology. The following research questions and objectives are to be answered and achieved, respectively, for the fulfillment of the research aim:

- How do elevated aerosol concentrations in an urban area influence clouds and precipitation not only in an urban area but also in an adjacent non-urban area?
- In what way does urban land use affect clouds and precipitation in both the urban and non-urban areas?
- How do spatial inhomogeneities in LT and aerosol concentrations between the urban and non-urban areas jointly affect clouds and precipitation in those areas?
- To simulate an MCS over the Seoul metropolitan region using a CSRM to assess the impacts of urbanization on clouds and precipitation not only in the urban area but also in the non-urban area.
- To isolate and quantify the individual and combined effects of urban aerosol concentrations and urban land use on clouds and precipitation in both the urban and non-urban areas.
- To examine process-level mechanisms how effects of urban aerosols and land use on clouds and precipitation in the urban area are tele-connected to those in the non-urban area.

2. Materials and methods

2.1. CSRM and its parameterizations

The Advanced Research Weather Research and Forecasting (ARW) model (version 3.3.1) serves as the CSRM in this study (Wang and Feingold, 2009). The ARW model, developed by the National Center for Atmospheric Research (NCAR) in collaboration with multiple institutions, including the National Oceanic and Atmospheric Administration and academic partners, is a widely used numerical weather prediction and atmospheric research tool. Its development began in the late 1990s to create a flexible, scalable, and computationally efficient model for both operational forecasting and research applications. The ARW model is a part of the broader weather research and forecasting framework, designed to replace older mesoscale models like the fifth-generation Penn State/NCAR

mesoscale model by incorporating advanced numerical techniques and modular physics parameterizations (Skamarock et al., 2008).

The ARW model is chosen for this study due to its robust capabilities in simulating MCSs. Its capability to adopt high-resolution grids enables the detailed representation of cloud and precipitation processes, critical for investigating the impacts of urban aerosols and land use. The model's flexible physics parameterization schemes, and particularly, its ability to integrate sophisticated microphysics schemes like the Hebrew University Cloud Model (HUCM) allow for explicit representation of aerosol-cloud interactions, which are central to this study. Additionally, the ARW model's compatibility with the Noah land surface model (Chen and Dudhia, 2001) facilitates accurate simulation of surface heat fluxes, essential for capturing urban land-use effects. The model's open-source availability, extensive community support, and proven performance in urban climate studies (e.g., Chen et al., 2015; Li et al., 2017) further justify its selection.

Compared to other CSRMs, such as the Regional Atmospheric Modeling System (RAMS) or the COnsortium for Small-scale MOdeling (COSMO), the ARW model offers several advantages. Unlike RAMS, which is computationally intensive and less modular, the ARW model provides a highly flexible framework with a wide range of physics options, making it suitable for both research and operational applications. COSMO, while effective for European climates, has less global community support and fewer aerosol-related parameterization options compared to the ARW model. Additionally, the ARW model's robust numerical solver and parallel computing capabilities ensure computational efficiency for high-resolution simulations.

The ARW model solves a set of fully compressible, non-hydrostatic governing equations in flux form, expressed in a terrain-following, hydrostatic-pressure vertical coordinate system (Skamarock et al., 2008). The model's core equations include:

Momentum equations:

$$\frac{\partial U}{\partial t}+\nabla\bullet\left(\vec{V}U\right)+\frac{\partial p}{\partial x}=F_u$$

$$\frac{\partial V}{\partial t}+\nabla\bullet\left(\vec{V}V\right)+\frac{\partial p}{\partial y}=F_v$$

$$\frac{\partial W}{\partial t}+\nabla\bullet\left(\vec{V}W\right)+\frac{\partial p}{\partial \eta}\bullet\frac{\partial \eta}{\partial z}=F_w-g$$

where U, V, and W are the momentum components in the x, y, and z directions, respectively; x and y represent the horizontal directions and z represents the vertical direction; η represents the terrain-following vertical coordinate; V is the three-dimensional velocity vector, i.e., (U, V, W); p is pressure; g is gravitational acceleration; F_u, F_v and F_w represent forcing terms (e.g., friction, Coriolis force, and subgrid-scale processes).

Continuity equation:

$$\frac{\partial \mu}{\partial t}+\nabla\bullet\left(\vec{V}\mu\right)=0$$

where μ is the dry air mass per unit area in a vertical column.

Thermodynamic equation:

$$\frac{\partial \Theta}{\partial t}+\nabla\bullet\left(\vec{V}\Theta\right)=F_\theta$$

where Θ is the potential temperature, and F_θ includes heating/cooling terms from radiation, latent heat, and diffusion.

Moisture equation:

$$\frac{\partial Q}{\partial t}+\nabla\bullet\left(\vec{V}Q\right)=F_q$$

where Q basically represents moisture variables (e.g., water-vapor and cloud-liquid mixing ratios), although it can represent other types of scalars such as aerosol concentrations. F_q includes source/sink terms from microphysical and aerosol processes. The equation

Table 1
Physical parameterizations, model configuration, input data, and associated physical processes and model components for the CSRM.

Physical processes and model components	Parameterizations, model configuration and input data	References
Shortwave and longwave radiation	RRTM	Fouquart and Bonnel, 1980; Mlawer et al., 1997
Microphysics with droplet and ice-crystal nucleation	Bin scheme utilizing the HUCM	Koop et al., 2000; Lohmann and Diehl, 2006; Möhler et al., 2006; Khain et al., 2011
Surface	Noah land surface model	Chen and Dudhia, 2001
Cumulus	None	
Resolutions	~200 m vertically and 500 m horizontally	
Number of vertical layers	100	
Model top pressure	50 hPa	
Synoptic-scale forcings	Met Office Unified Model	Brown et al., 2012
Boundary condition	Open lateral	

set is solved using a time-split integration scheme with a third-order Runge-Kutta method for numerical stability and accuracy.

Important physical parameterizations, model configuration and input data for the CSRM are summarized in Table 1 below. The HUCM bin scheme (Table 1) solves a set of kinetic equations to represent size distribution functions for seven classes of hydrometeors and aerosols acting as cloud condensation nuclei (CCN) and ice nucleating particles (INPs). Consequently, there are seven distinct size distribution functions for hydrometeors, which include drops, three types of ice crystals or cloud ice (plates, columns, and dendrites), snow aggregates or snow, graupel, and hail. Drops with a radius smaller than 40 μm are classified as droplets or cloud liquid, while those larger than 40 μm are considered raindrops or rain. This bin scheme calculates the effective sizes of hydrometeors, which are then input into the Rapid Radiative Transfer Model (RRTM) (Table 1), allowing the model to simulate how these effective sizes influence radiation.

There are two size distribution functions for aerosols, which include CCN and INPs. The background properties (e.g., concentration, size distribution and composition) of INPs, which act as sources of ice-crystal nucleation, are identical to those of CCN, which act as sources of droplet nucleation, with the exception that the concentration of background CCN is 100 times greater than that of background INPs. This difference reflects the general disparity in concentrations between CCN and INPs, as noted by Pruppacher and Klett (1978).

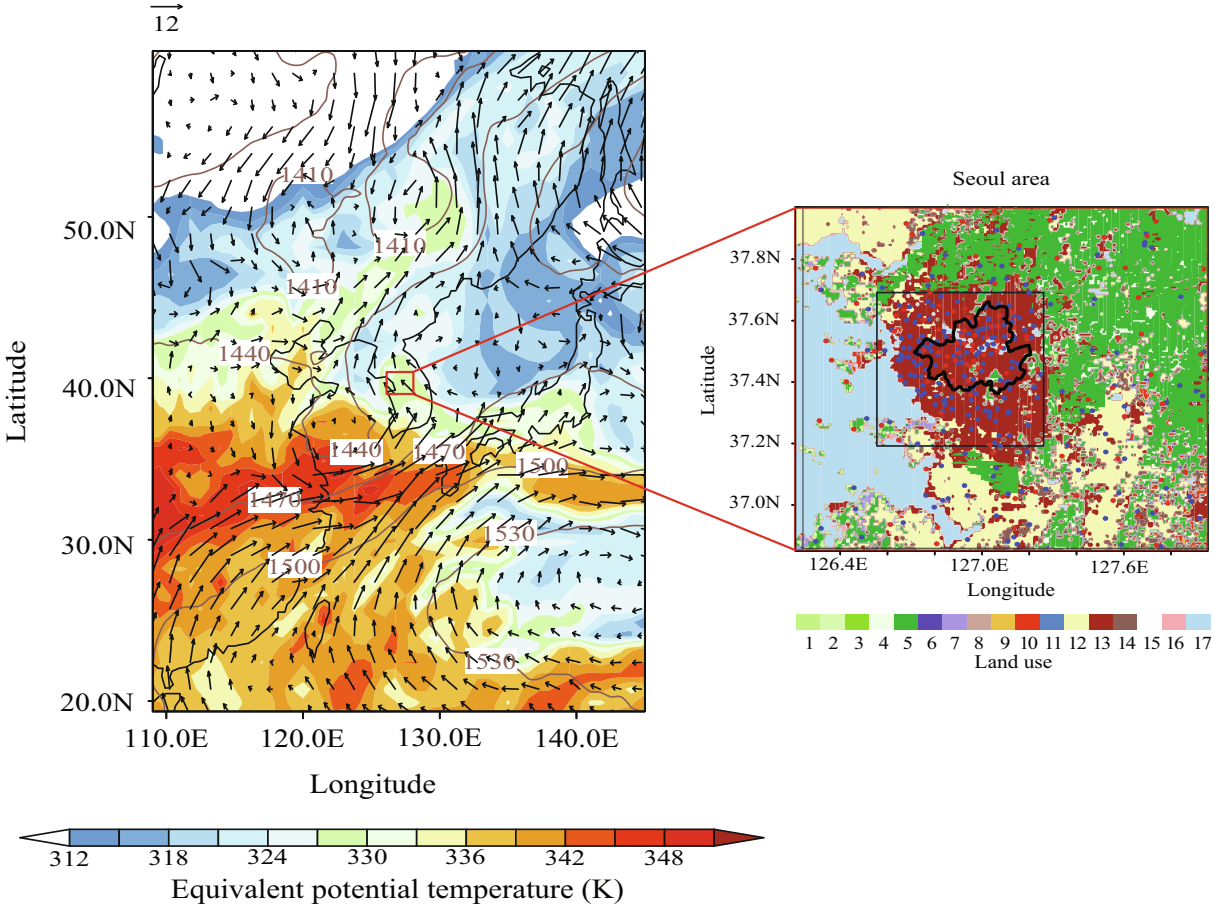

Fig. 1. The left panel shows the 850 hPa wind (m s^{-1}, arrows), geopotential height (m, contours), and equivalent potential temperature (K, shaded) at 10:00 LST on June 22nd, 2016 over northeastern Asia. The rectangle on the Korean Peninsula marks the domain of the Seoul metropolitan region and this rectangle is enlarged in the right panel. The inner rectangle in the right panel outlines the urban area, while the surrounding area outside the rectangle represents the non-urban area. For reference, the boundary of the Seoul city, the biggest and most populated city among cities in the region, is marked by the closed contour within the inner rectangle. In the right panel, blue dots mark the locations where precipitation is measured, while red dots mark those where aerosol properties are measured. In the right panel, each number beneath a specific colour in the colour bar corresponds to a different land use category as follows: 1. Evergreen needleleaf forest; 2. Evergreen broadleaf forest; 3. Deciduous needleleaf forest; 4. Deciduous broadleaf forest; 5. Mixed forests; 6. Closed shrublands; 7. Open shrublands; 8. Woody savanna; 9. Savannas; 10. Grasslands; 11. Permanent wetlands; 12. Croplands; 13. Urban and built-up; 14. Cropland/natural vegetation mosaic; 15. Snow and ice; 16. Barren or sparsely vegetated; 17. Water. (For interpretation of the references to colour in this figure legend, the reader is referred to the web version of this article.)

2.2. Aerosol preprocessor and properties

Aerosol preprocessor, which is capable of incorporating the spatiotemporal variation of aerosol properties by interpolating or extrapolating observed background aerosol data—such as aerosol mass concentration (e.g., PM2.5 and PM10)—into the model's grid points and time steps, is implemented in the ARW model. Here, "PM" refers to particulate matter, where PM2.5 (PM10) represents the mass of aerosols with diameters smaller than 2.5 μm (10.0 μm) per unit volume of air. In this study, the inverse distance weighting method is applied for the interpolation and extrapolation of aerosol data into the model grid and time steps.

Surface observation sites that measure aerosol properties are present within the domain of the Seoul metropolitan region (Fig. 1). Note that the domain length spans 171 km in the east-west direction and 122 km in the north-south direction. These sites are categorized into two types. The distance between sites in the first type varies from approximately 1 km to 10 km, with a time interval of about ten minutes between measurements. Over 90% of the sites belong to this first category. These first-type sites specifically measure PM2.5 and PM10 but do not monitor other aerosol properties, such as composition and size distribution. Less than 10% of the observation sites fall into the second category. These second-type sites are a part of the Aerosol Robotic Network (AERONET; Holben et al., 2001) and are equipped to measure aerosol composition and size distribution. Data from the first-type sites is used to represent the spatiotemporal variability of aerosols across the domain and during the simulation. In contrast, data from the AERONET sites are employed to characterize aerosol composition and size distribution.

The AERONET data are averaged over the AERONET sites at 12:00 LST on June 22nd, 2016, which is one hour prior to the formation of the observed MCS. Based on this average data, it is assumed that the aerosol particles are internally mixed with 65% ammonium sulfate and 35% organic compounds throughout the domain and simulation period. This mixture is considered representative of the aerosol composition across the domain and throughout the simulation period. Since ammonium sulfate and organic compounds are key components of CCN, it is assumed that the PM2.5 and PM10 data from the first-type sites represent the mass concentration of aerosols that act as CCN in the domain. Aerosols reflect, scatter, and absorb both shortwave and longwave radiation before being activated; however, these aerosol-radiation interactions are not accounted for in this study. This omission is primarily due to the negligible presence of radiation absorbers in the mixture, with black carbon being the most significant radiation absorber.

The average AERONET data indicate that the size distribution of background aerosols follows a bi-modal log-normal distribution. It is assumed that this size distribution, characterized by specific parameters (i.e., modal radius, standard deviation for both accumulation and coarse modes, and the partition of aerosol number between these modes), remains consistent across the domain and simulation period. The modal radii for the distribution are 0.120 and 1.511 μm, while the standard deviations are 1.48 and 1.81 for the accumulation and coarse modes, respectively. The partition of aerosol number, normalized by the total aerosol count in the distribution, is 0.999 for the accumulation mode and 0.001 for the coarse mode. Using PM2.5 and PM10 data from the first-type sites, along with interpolated and extrapolated values at grid points just above the surface and across time steps, the background number concentrations of aerosols acting as CCN are derived based on the previously mentioned assumptions about aerosol composition and size distribution, which are informed by AERONET data.

There is no variation in the background concentrations of aerosols acting as CCN from just above the surface to the top of the planetary boundary layer (PBL). However, it is assumed that these concentrations decrease exponentially with height above the PBL. The size distribution and composition of aerosols acting as CCN remain constant with height. Once the background aerosol properties are assigned to each grid point and time step, they do not change throughout the simulation period.

2.3. Aerosol processes and recovery method

Once clouds form and background aerosols are included in them, these aerosols no longer function as background aerosols. Their size distribution and concentration begin to change due to various aerosol sinks and sources, such as advection and aerosol activation (Fan et al., 2009). For instance, once aerosols are activated, they are removed from their corresponding bins in the aerosol spectra. Within clouds, following activation, aerosol mass becomes incorporated into hydrometeors, where it is transferred to different types and sizes of hydrometeors through collision and collection. Ultimately, aerosol mass is eliminated from the atmosphere when hydrometeors containing aerosol mass reach the surface.

In non-cloudy areas, the size and spatial distributions of aerosols are intended to match those of the background aerosols. This approach is referred to as the "aerosol recovery method" and implemented in the ARW model. In this method, immediately after clouds completely dissipate at any given grid point, the aerosol size distribution and number concentration return to the background properties that existed prior to the inclusion of the grid point in clouds. This allows us to maintain the concentrations of background aerosols outside of clouds in the simulation, aligning them with observed values. As a result, the spatiotemporal distributions of background aerosols in the simulation replicate the observed distributions throughout the domain and simulation period, particularly in relation to real-world aerosol spatiotemporal inhomogeneity, especially regarding that between the urban and non-urban areas.

In the aerosol recovery method, there is no time lag between cloud dissipation and aerosol recovery. A grid point is considered to be in clouds when the total mass of all hydrometeor types—such as drops, cloud ice, snow, graupel, and hail—is greater than zero. Once this total mass reaches zero, clouds are deemed to have disappeared. Numerous studies utilizing the CSRM have implemented this aerosol recovery method, demonstrating that it facilitates reasonable simulations of overall cloud and precipitation properties (e.g., Morrison and Grabowski, 2011; Lebo and Morrison, 2014; Lee et al., 2016; Lee et al., 2018; Sterzinger et al., 2022).

2.4. Flux of the moist static energy (MSE)

To better understand impacts of urbanization on clouds and precipitation, the flux of the MSE is calculated in this study as follows:

$$\overrightarrow{Fs} = S\,\rho\,\overrightarrow{U}$$

where $\overrightarrow{Fs}$ represents the flux of the MSE, S the MSE, ρ the air density and $\overrightarrow{U}$ the horizontal-wind vector, i.e., (U, V). In this equation, the flux is expressed in the vector form consisting of both magnitude and direction.

3. Case description

The urban core or area of the Seoul metropolitan region comprises the Seoul city and several adjacent cities such as Incheon and Suwon, and these cities collectively form one of the most urbanized and populous areas in East Asia (Fig. 1; Lee et al., 2018). In contrast, the adjacent non-urban area consists primarily of forested and agricultural land with minimal built-up surface (Fig. 1). This sharp urban–non-urban gradient provides a good natural setting for examining the impacts of land use and associated LT disparity between the urban and non-urban areas on clouds and precipitation. Ground-based air quality monitoring sites within the region (Fig. 1) provide spatiotemporal coverage of aerosol properties including aerosol concentrations and showed notably elevated concentrations in the urban core compared to the surrounding area. This indicates that the Seoul metropolitan region is suitable for examining the impacts of aerosol disparity between the urban and non-urban areas on clouds and precipitation.

At 10:00 LST on June 22nd, 2016, which is three hours prior to the formation of the observed MCS, synoptic-scale features favorable for convection over the Korean Peninsula are evident (Fig. 1). The western Pacific subtropical high was positioned southeast of the peninsula, and a low-pressure trough lies over northern China. A southwesterly low-level jet between these systems transported warm, moist air into the southern Korean Peninsula, where high equivalent potential temperature and convergence were observed (Fig. 1). Although these features were not centered over the Seoul metropolitan region, they contributed indirectly to the development of the MCS there by supporting a northward transport of warm, moist air from the southern Peninsula into the region (Fig. 1).

The observed MCS is selected for this study, because it exhibited strong convective development and heavy precipitation. During the MCS event, rainfall was widespread, with a peak precipitation rate reaching 65 mm hr^{-1}, as recorded by the Korea Meteorological Administration (KMA). Precipitation data were obtained from automatic weather stations (King, 2009), operated by the KMA and providing hourly observations at a spatial resolution ranging from ~1 km to ~10 km (Fig. 1). These high-resolution observations support robust validation of the simulation results.

4. Simulations

The control run, which is a three-dimensional CSRM simulation of the observed MCS, is performed over the domain of the Seoul metropolitan region (Fig. 1) and the six-hour period during which the MCS was observed in the domain. Here, areas with water body in the domain are excluded from the analysis of results.

In the control run, the average background aerosol concentration is 8890 cm^{-3} in the urban area and 2301 cm^{-3} in the non-urban area, indicating higher aerosol loading in the urban core (Table 2 and Fig. 2). To isolate the impact of this difference, we repeat the control run by reducing the urban aerosol concentration at each grid point and time step by a specific factor so that the urban average matches the non-urban value (2301 cm^{-3}). This simulation is referred to as the no_ub_aro run (Table 2 and Fig. 2). Comparisons between the control and no_ub_aro runs assess the influence of elevated urban aerosol concentrations and the spatial inhomogeneity of aerosol concentrations on clouds and precipitation.

To examine land use effects, we also conduct the no_ub_sfc run, in which built-up urban land is replaced with mixed forest, the dominant non-urban land cover (Table 2 and Fig. 2). Comparisons between the control and no_ub_sfc runs highlight impacts of urban land use and its spatial variability.

5. Results

5.1. Precipitation rate and cumulative precipitation

The control run, incorporating elevated aerosol concentrations, closely reproduces the observed temporal evolution of precipitation rates in both the urban and non-urban areas (Fig. 3). In the urban area, the control run consistently yields higher precipitation

Table 2
Summary of simulations.

Simulations	The average background aerosol concentration (cm^{-3})		Land use	
	Urban area	Non-urban area	Urban area	Non-urban area
Control run	8890	2301	Built-up	Mostly mixed forest
No_ub_aro run	2301	2301	Built-up	Mostly mixed forest
No_ub_sfc run	8890	2301	Mixed forest	Mostly mixed forest

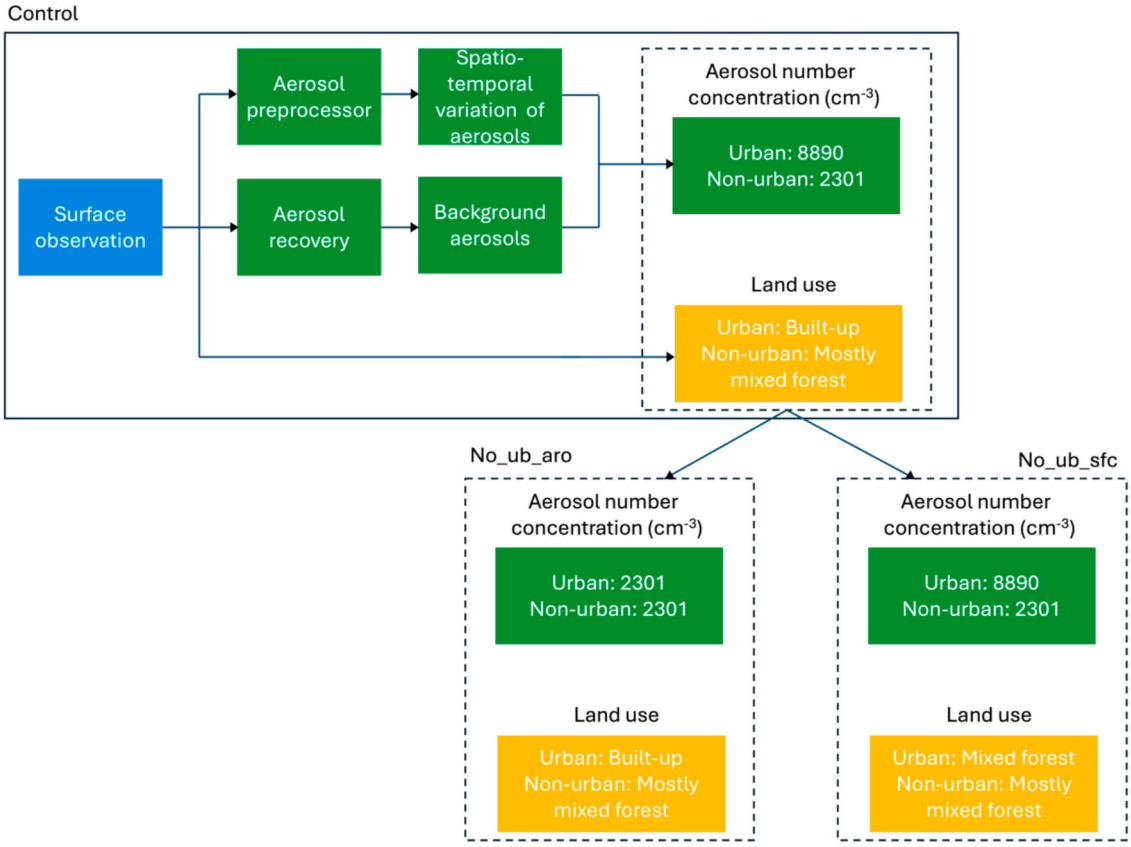

Fig. 2. Flowchart summarizing the experimental structure and design of simulations.

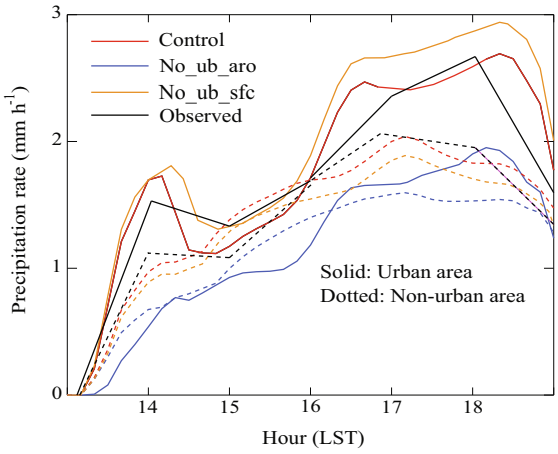

Fig. 3. Time series of simulated precipitation rates at the surface, which are averaged over the urban and non-urban areas of the domain and smoothed with a one-hour running average, for the control, no_ub_aro and no_ub_sfc runs. The averaged and observed surface precipitation rates over observation sites in each of those areas are also shown.

rates than the no_ub_aro run (with reduced aerosols). Precipitation is negligible around 13:00 LST, but by ~14:00 LST, the control run reaches ~2 mm hr^{-1}, about twice the rate of the no_ub_aro run. This gap briefly narrows as the control run declines sharply while the no_ub_aro run increases gradually between ~14:00 and ~ 14:30 LST, then widens again from ~16:00 LST onward, as precipitation in the control run intensifies between ~16:00 and ~ 16:30 LST. Both the runs reach their peak around 18:30 LST, with the peak in the control run approximately 1 mm hr^{-1} higher. Afterward, differences diminish. In the non-urban area, a similar overall pattern emerges, with the control run producing higher precipitation rates, though the peak occurs earlier—around 17:00 LST—roughly one

hour and half before the urban peak. Unlike the urban area, the difference grows steadily without abrupt shifts until the peak is reached. Consistent with patterns in the precipitation rates, the domain-averaged cumulative precipitation at the last time step in the control run exceeds that of the no_ub_aro run in both the urban and adjacent non-urban areas: 12.3 mm vs. 8.2 mm in the urban area,

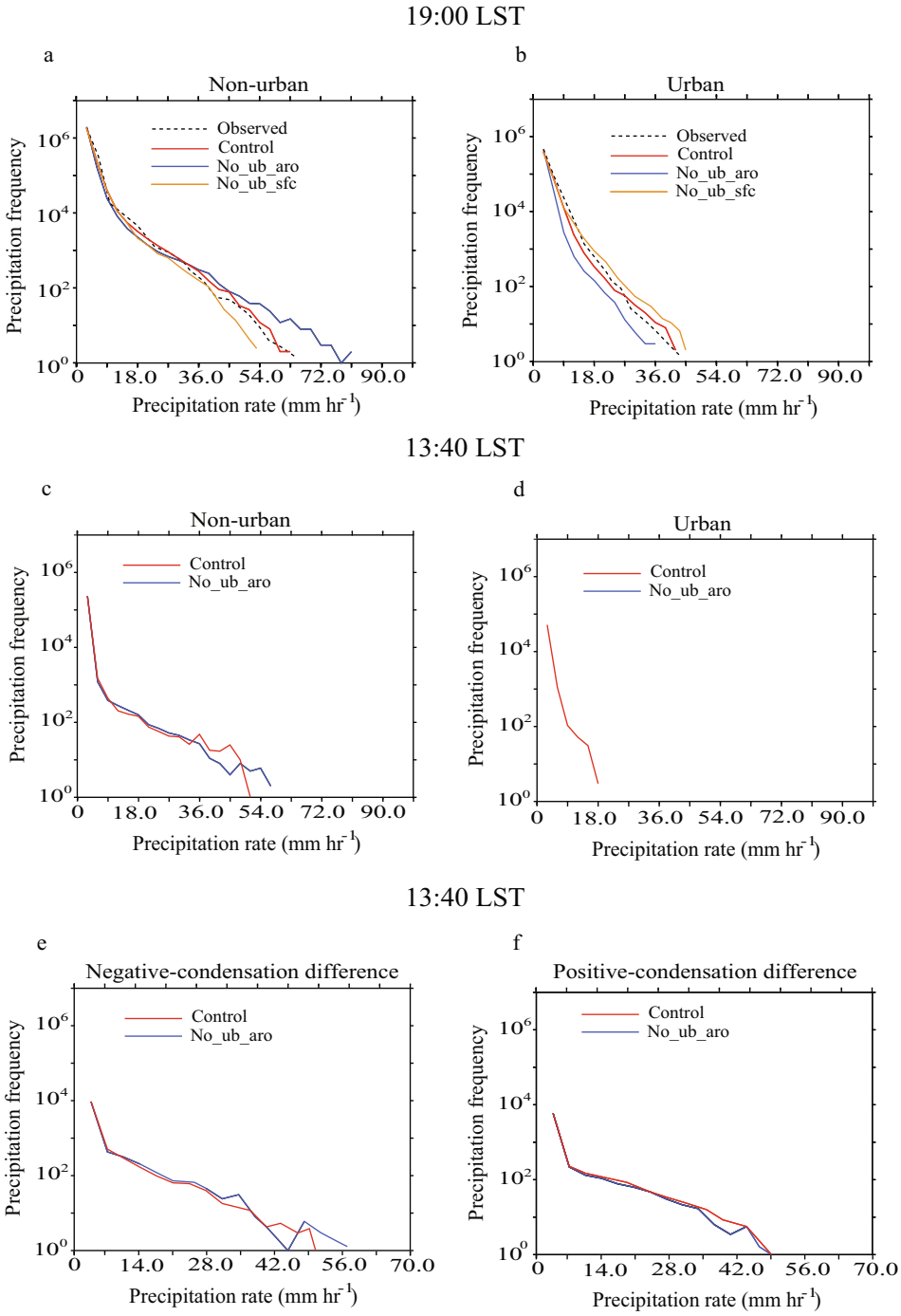

Fig. 4. Cumulative frequency distributions of the precipitation rates at the surface at (a) and (b) 19:00 LST, which corresponds to the last time step, (c), (d), (e) and (f) 13:40 LST, (g), (h), (i) and (j) 13:50 LST, and (k) and (l) 14:10 LST. (a), (c), (g) and (k) are for the non-urban area, while (b), (d), (h) and (l) are for the urban area. (e), (f), (i), and (j) are for the non-urban area. (e) and (i) are for zones of negative-condensation differences where the control run shows reduced condensation, while (f) and (j) are for zones of positive-condensation differences where the control run shows enhanced condensation, relative to the no_ub_aro run. These zones are included in the red rectangle in Fig. 5. (For interpretation of the references to colour in this figure legend, the reader is referred to the web version of this article.)

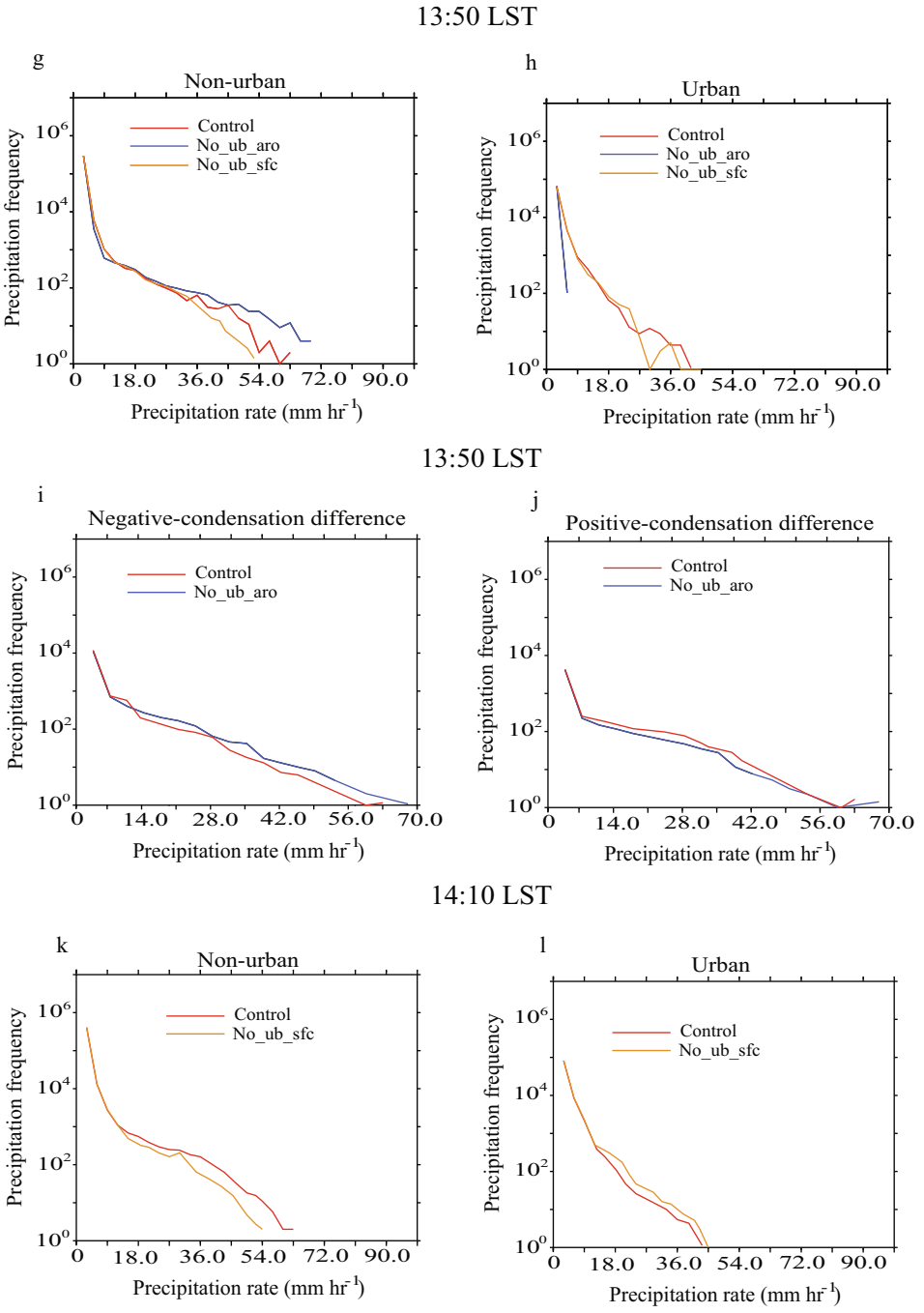

Fig. 4. (*continued*).

and 10.3 mm vs. 8.1 mm in the non-urban area.

When urban land use is replaced by the dominant non-urban counterpart (no_ub_sfc run), precipitation in the urban area surpasses that in the control run throughout the simulation (13.7 mm vs. 12.3 mm; the domain-averaged cumulative rainfall at the last time step) (Fig. 3). Whereas, the control run produces more rainfall in the non-urban area (10.3 mm vs. 9.4 mm). Despite these magnitude differences, the timing of precipitation remains similar in the urban area: both runs show negligible rainfall around 13:00 LST, a sharp increase around 14:00 LST, a temporary decline between ~14:00 and ~ 14:30 LST, renewed growth around ~16:00–16:30 LST, a gradual rise between ~16:30 LST and the occurrence of the peak precipitation around 18:30 LST, and another decline after the peak. In the non-urban area, both runs display smoother, slower variations and nearly identical timing. The magnitude gap slowly widens until both reach peak rainfall around 17:00 LST. The results here indicate that both urban aerosols and land use modulate precipitation not

only in the urban area but also in the non-urban area. This highlights the teleconnection, whereby precipitation changes in the urban area, driven by urban aerosols and land use, influences precipitation beyond the urban boundary.

5.2. *Precipitation frequency distributions and their governing mechanisms*

Cumulative frequency distributions of precipitation rates at the final timestep (19:00 LST) reveal distinct effects driven by urban aerosols and land use (Fig. 4a and b). The observed maximum precipitation rates are 44 and 65 mm hr^{-1} in the urban and non-urban areas, respectively, closely matching those in the control run (Fig. 4a and b). Overall, the observed frequency distribution matches the

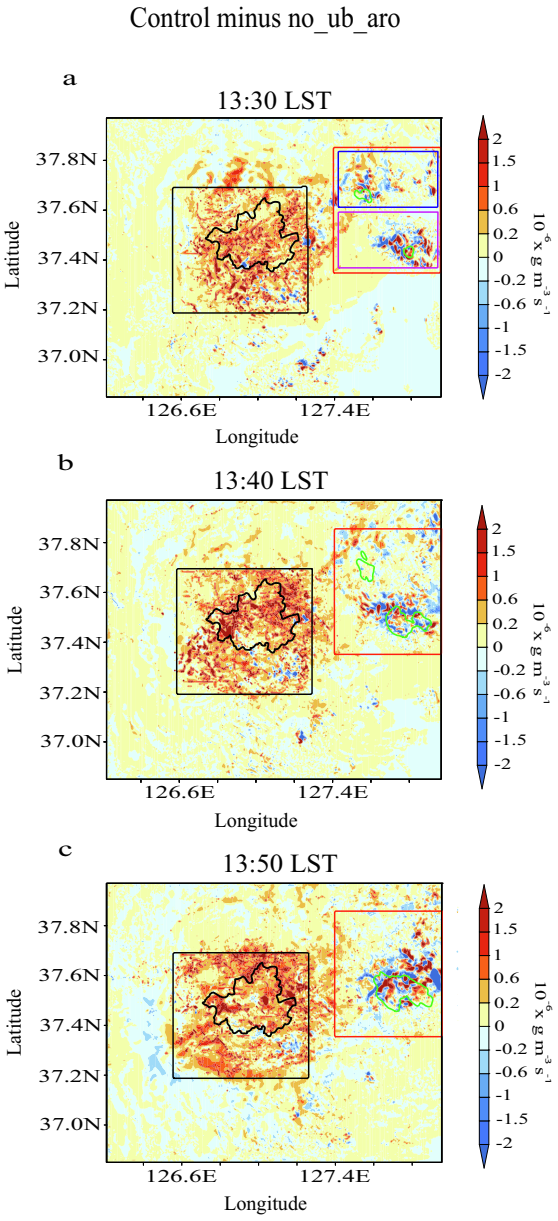

Fig. 5. Spatial distributions of differences in condensation rates between the control and no_ub_aro runs at (a) 13:30, (b) 13:40, and (c) 13:50 LST. These differences are shaded. Dark-green contours represent precipitation rates at 12 mm hr^{-1} in the no_ub_aro run. The inner black rectangle, which outlines the urban area, and the closed contour, which is within the black rectangle and marks the boundary of the Seoul city, are the same as in the right panel of Fig. 1. The red rectangle marks the region where zones with lower condensation rates neighbor those with higher condensation rates in the control run. At (a) 13:30 LST, the red rectangle includes two representative sub-regions with those zones: the upper and lower ones are outlined by the blue and purple rectangles, respectively. (For interpretation of the references to colour in this figure legend, the reader is referred to the web version of this article.)

control run, demonstrating its validity.

In the non-urban area, the control run shows higher frequencies for precipitation with rates between 2 and 33 mm hr^{-1}, corresponding to light, moderate, heavy and very heavy precipitation according to the KMA classification, but lower frequencies for rates > 33 mm hr^{-1}, which fall within very heavy category, compared to the no_ub_aro run (Fig. 4a). In this study, following the KMA criteria, precipitation rates of < 3 mm hr^{-1} are classified as "light", 3–15 mm hr^{-1} as "moderate", 15–30 mm hr^{-1} as "heavy", and > 30 mm hr^{-1} as "very heavy" (Korean Meteorological Administration, 2025).

Here, 33 mm hr^{-1} acts as a tipping precipitation rate where lower frequency turns into higher one in the no_ub_aro run. Notably, precipitation rates exceeding 63 mm hr^{-1} are absent in the control run but present in the no_ub_aro run, with the no_ub_aro run's frequency at 63 mm hr^{-1} being ~10 times higher. This suggests that urban aerosols suppress the occurrence of very heavy precipitation in the non-urban area. The lower frequency at higher rates is outweighed by the higher frequency at lower rates, which results in the greater cumulative precipitation in the control run than in the no_ub_aro run over the non-urban area. On the other hand, the control run shows higher frequencies across all precipitation with rates that range from 2 to 63 mm hr^{-1}, corresponding to light to very heavy precipitation, and this is consistent with larger cumulative rainfall in the control run than the no_ub_sfc run for the non-urban area (Fig. 4a). This means that urban land use intensifies light to very heavy precipitation in the non-urban area.

In the urban area, the cumulative precipitation frequency at the last time step is consistently higher across all precipitation with rates from 3 to 43 mm hr^{-1}, corresponding to moderate to very heavy precipitation, in the control run compared to the no_ub_aro run (Fig. 4b). This indicates that urban aerosols intensify urban moderate, heavy and very heavy precipitation, resulting in the greater cumulative precipitation in the control run for the urban area. Conversely, the no_ub_sfc run exhibits a consistently higher frequency across all precipitation with rates from 3 to 45 mm hr^{-1}, also corresponding to moderate to very heavy precipitation (Fig. 4b). Consequently, the no_ub_sfc run produces greater cumulative precipitation than the control run for the urban area, meaning that urban land use suppresses urban moderate, heavy and very heavy precipitation.

The temporal evolution of precipitation frequencies provides deeper insight (Fig. 4). In the non-urban area, precipitation initiates at 13:30 LST and, as precipitation intensifies with time, at 13:40 LST, the no_ub_aro run exhibits higher frequencies for rates from 9 to 35 mm hr^{-1} and above 48 mm hr^{-1} than the control run, while the control run dominates for rates <9 mm hr^{-1} and between 35 and 48 mm hr^{-1} over the no_ub_aro run with the maximum precipitation rate of ~60 mm hr^{-1} between the runs (Fig. 4c). By 13:50 LST, a tipping point at 12 mm hr^{-1} emerges, with the no_ub_aro run showing higher frequencies above the tipping point and lower frequencies below it than the control run (Fig. 4g). A distinct region—highlighted by a red rectangle—shows adjacent zones of higher and lower rates of condensation, which is a primary source of cloud liquid, rain and precipitation, in the control run than in the no_ub_aro run (Fig. 5). This region coincides with areas of precipitation with rate > 12 mm hr^{-1} in the no_ub_aro run as time progresses to 13:50 LST (Fig. 5). The tipping point shifts to 33 mm hr^{-1} by the final timestep (Fig. 4a and g). In the urban area, precipitation forms by 13:40 LST, with the control run maintaining higher frequencies across all rates from 13:50 LST onward than the no_ub_aro run (Fig. 4d and h). This is associated with widespread stronger condensation in the control run than in the no_ub_aro run (Figs. 4h and 5).

At 13:50 LST, the control run dominates for higher rates (> 33 mm hr^{-1}) over the no_ub_sfc run in the non-urban area, while the no_ub_sfc run shows higher frequencies in the urban area for mid-range rates (15–27 mm hr^{-1}) than the control run (Fig. 4g and h). By 14:10 LST, the characteristic differences between the runs are well established: the control run shows consistently higher frequencies across all intensities than the no_ub_sfc run in the non-urban area (Fig. 4k), and the no_ub_sfc run exhibits higher frequencies for all precipitation rates than the control run in the urban area (Fig. 4l), mirroring the patterns observed at the final timestep (Fig. 4a and b).

To further explore differences in precipitation frequency between the control and no_ub_aro runs, we obtain the flux of the MSE over the PBL and the red-rectangle region, as the MSE in the PBL generally exerts a stronger influence on instability and updrafts than that above the PBL (Fig. 6a, d and g). For the exploration between the control and no_ub_sfc runs, the net summed flux of MSE across the boundary between urban and non-urban areas—defined by the inner rectangle in the right panel of Fig. 1—is calculated in the PBL from 13:30 to 14:10 LST.

At 13:30 LST, the control run exhibits stronger MSE fluxes from the upper and lower sub-regions toward the urban area compared to the no_ub_aro run (Figs. 5a and 6d), reflecting enhanced updrafts, convection and convergence in the urban area. The average updraft mass flux over the troposphere and simulation period in the urban area is 8.2×10^{-2} and 6.1×10^{-2} kg m^{-2} s^{-1} in the control and no_ub_aro runs, respectively. In the urban area, the higher aerosol concentrations increase CCN concentrations, promoting droplet nucleation and elevating cloud droplet number concentration (CDNC), an associated integrated droplet surface area where water vapor condense in the control run as compared to the situation in the no_ub_aro run; CDNC, which is averaged over grid points and time steps with non-zero CDNC in the urban area, is 893 cm^{-3} in the control run and 211 cm^{-3} in the no_ub_aro run. This raises rates of condensation and associated latent-heat release as a source of buoyancy in the control run, eventually resulting in stronger updrafts and convergence in the urban area for the control run. These elevated MSE fluxes and associated convergence (Fig. 6d, green oval) indicate more efficient transport of convective energy toward the urban area. Relative to 13:15 LST, in the sub-regions, this intensification expands adjacent zones of both reduced and increased instability and condensation in the control run (Fig. 6a and d). As a result, the spatial contrasts in condensation between the control and no_ub_aro runs become more pronounced by 13:30 LST, leading to substantial differences in cloud liquid and rain content (Fig. 6a, b, c, d, e and f).

From 13:30 to 13:50 LST, the contrasts in condensation intensify, particularly in the lower sub-region, with affected areas expanding over time (Fig. 6d and g). In the expanding zones of negative-condensation differences, the no_ub_aro run exhibits more condensation, resulting in overall greater cloud liquid and rain than the control run between 13:30 and 13:50 LST (Fig. 6e and h). Correspondingly, at 13:40 LST, the no_ub_aro run shows higher cumulative precipitation frequency for rates above 9 mm hr^{-1}—except between 36 and 47 mm hr^{-1} (Fig. 4e). By 13:50 LST, this trend becomes more pronounced, with the no_ub_aro run displaying greater frequency for all precipitation rates above 12 mm hr^{-1}, though there is lower frequency for precipitation below this threshold than in

Control minus no_ub_aro

Condensation rate and MSE fluxes | Negative-condensation difference | Positive-condensation difference

13:15 LST

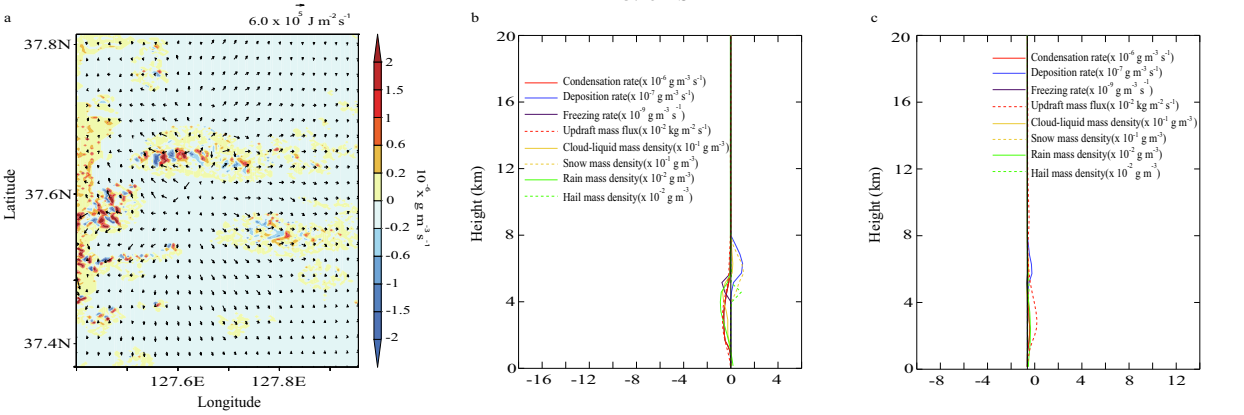

13:30 LST

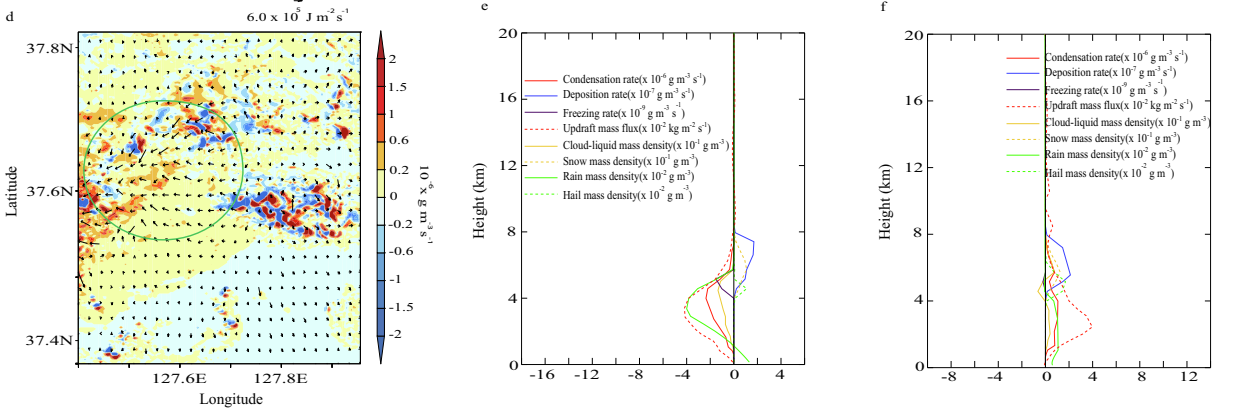

13:50 LST

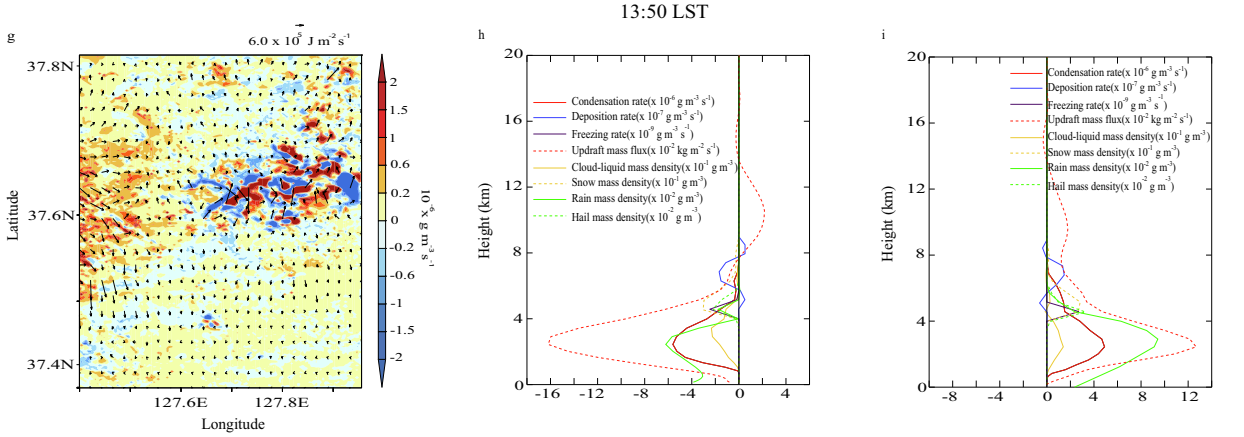

(caption on next page)

Fig. 6. Spatial distributions of differences in condensation rates and MSE fluxes, and vertical distributions of differences in the domain-averaged condensation, deposition and freezing rates, and cloud-liquid, rain, snow and hail mass density, and updraft mass fluxes between the control and no_ub_aro runs in the red-rectangle region in Fig. 5. (a), (b) and (c) are for 13:15 LST, (d), (e) and (f) for 13:30 LST, and (g), (h) and (i) for 13:50 LST. (a), (d) and (g) are those spatial distributions where differences in condensation rates are shaded and those in MSE fluxes are represented by vector arrows. Here, MSE fluxes are averaged over the PBL. The green oval in (d) marks the enhanced MSE fluxes toward the urban area in the control run. (b), (e) and (h) are those vertical distributions for zones of negative-condensation differences, while (c), (f) and (i) are for zones of positive-condensation differences. (For interpretation of the references to colour in this figure legend, the reader is referred to the web version of this article.)

the control run (Fig. 4i).

Conversely, in the expanding zones of positive-condensation differences, the control run maintains greater condensation, and overall, more cloud liquid and rain, along with greater precipitation frequency across almost all intensity ranges during the period between 13:30 and 13:50 LST than the no_ub_aro run (Figs. 4f, j, 6f and i). However, at 13:50 LST, the increase in the frequency of precipitation with rates above 12 mm hr^{-1} for the negative-difference zones in the no_ub_aro run outweighs the decrease in the positive-difference zones, yielding overall higher frequency of precipitation above 12 mm hr^{-1} across the non-urban area (Fig. 4g, i and j). Meanwhile, the consistent suppression of precipitation rates below 12 mm hr^{-1} in both zones contributes to a net decrease in the frequency for those rates in the no_ub_aro run (Fig. 4g, i and j).

The net summed MSE flux over the period between 13:30 and 14:10 LST is 6.5×10^8 and 9.1×10^8 J m^{-2} s^{-1} in the control and no_ub_sfc runs, respectively. The flux from the non-urban area to the urban area has a positive sign, while the flux from the urban area to the non-urban area has a negative sign. Hence, this indicates that MSE consistently flows into the urban area in both the control and no_ub_sfc runs but more intensely in the no_ub_sfc run. This enhanced MSE transport in the no_ub_sfc run reflects stronger urban updrafts and convection, which induce greater low-level convergence toward the urban area. The stronger urban updrafts are primarily due to higher surface latent-heat fluxes (30.2 vs. 11.3 W m^{-2}), which compensate for lower sensible-heat fluxes (6.5 vs. 12.7 W m^{-2}) and induce a greater amount of near-surface water vapor in the no_ub_sfc run than in the control run. The greater amount of near-surface water vapor eventually results in the higher equivalent potential temperature (341.6 vs. 340.8 K at 2 m altitude) and convective available potential energy (CAPE), leading to the stronger updrafts; the numbers in the parentheses are the time- and domain-averaged values. The increased inflow of MSE fuels even more vigorous convection and leads to even stronger updrafts in the no_ub_sfc run. The average updraft mass flux over the troposphere and simulation period in the urban area is 8.2×10^{-2} and 9.3×10^{-2} kg m^{-2} s^{-1} in the control and no_ub_sfc runs, respectively. This in turn leads to larger hydrometeor mass and higher precipitation frequency in the urban area for the no_ub_sfc run (Fig. 4b). Conversely, the resulting outflow of MSE from the non-urban area suppresses convection there, reducing precipitation frequency in the no_ub_sfc run (Fig. 4a).

Table 3
Summary of the three main simulations (control, no_ub_aro and no_ub_sfc runs) and their repeated runs. The main simulations have the time- and domain-averaged CAPE of 1800 J kg^{-1} and wind shear of 10 m s^{-1} in synoptic-scale forcings. The main simulations are repeated with the average CAPE reduced to 900 J kg^{-1} (control_LC, no_ub_aro_LC and no_ub_sfc_LC) and increased to 3600 J kg^{-1} (control_HC, no_ub_aro_HC and no_ub_sfc_HC), and with the average wind shear altered to 5 m s^{-1} (control_LW, no_ub_aro_LW and no_ub_sfc_LW) and 15 m s^{-1} (control_HW, no_ub_aro_HW and no_ub_sfc_HW). The magnitude of these variations of CAPE and wind shear is based on Weisman and Klemp (1982). Cumulative precipitation refers to the domain-averaged value at the final time step for the urban and non-urban areas. In each set of the repeated runs, cumulative precipitation frequency at the final time step is compared between the runs with different aerosol concentrations but identical land use, which is similar to the comparison between the control and no_ub_aro runs as in Fig. 4a, for the non-urban area. In this comparison, the tipping precipitation rate—where frequency in the run with the higher aerosol concentration becomes lower than in the run with the lower aerosol concentration—is identified and reported for each set.

Simulations	Synoptic-scale forcings		Cumulative precipitation (mm)		Non-urban area
	CAPE (J kg^{-1})	Wind shear (m s^{-1})	Urban area	Non-urban area	Tipping precipitation rate (mm hr^{-1})
Control run	1800	10	12.3	10.3	33
No_ub_aro run	1800	10	8.2	8.1	
No_ub_sfc run	1800	10	13.7	9.4	
Control_LC run	900	10	7.5	6.3	36
No_ub_aro_LC run	900	10	5.3	5.0	
No_ub_sfc_LC run	900	10	8.6	5.7	
Control_HC run	3600	10	22.2	19.5	28
No_ub_aro_HC run	3600	10	15.2	15.0	
No_ub_sfc_HC run	3600	10	24.5	17.8	
Control_LW run	1800	5	12.1	10.0	34
No_ub_aro_LW run	1800	5	7.8	7.5	
No_ub_sfc_LW run	1800	5	13.5	9.1	
Control_HW run	1800	15	12.7	10.8	32
No_ub_aro_HW run	1800	15	8.6	8.6	
No_ub_sfc_HW run	1800	15	14.1	9.8	

5.3. Sensitivity to stability and wind shear

As demonstrated by Weisman and Klemp (1982), Lee et al. (2008) and Fan et al. (2009), the development of clouds and their interactions with aerosols and surface fluxes is strongly dependent on stability and wind shear. Based on this, to assess the robustness and generalizability of the simulation results, sensitivity tests are conducted by repeating the three main simulations (control, no_ub_aro, and no_ub_sfc runs) under varying stability, which is represented by CAPE, and wind shear. The variation of CAPE is performed by increasing or decreasing the PBL temperature, which is in synoptic-scale forcings, at each grid point and time step by a certain factor. Following Weisman and Klemp (1982), wind shear is defined to be the difference between the mean horizontal wind speed over the lowest 6 km of the profile and the average wind speed over the lowest 500 m. With this definition, the variation of the wind shear is performed by increasing or decreasing the horizontal wind speed, which is again in synoptic-scale forcings, at each grid point and time step by a certain factor between 500 m and 6 km in altitude. The summary of the main simulations as well as sensitivity tests in terms of their CAPE, wind shear and precipitation characteristics is given in Table 3.

Despite the variations of CAPE and wind shear, the key patterns identified in the main simulations are preserved (Table 3). For example, in all scenarios, the run with the higher aerosol concentration in the urban area (e.g., the control run) consistently produces greater cumulative precipitation in both the urban and non-urban areas compared to the run with the lower aerosol concentration (e.g., the no_ub_aro run) when land use is identical between the runs. The run with built-up urban land use replaced by the dominant non-urban counterpart (e.g., the no_ub_sfc run) continues to enhance urban precipitation while reducing non-urban precipitation, relative to the run with built-up urban land use (e.g., the control run) when the runs have identical aerosol concentrations (Table 3).

Moreover, across all CAPE and wind shear conditions, the tipping precipitation rate, which is discussed in Section 5.2, forms in the non-urban area, although the tipping rate shows a variation with CAPE and wind shear (Table 3). This suggests that the redistribution of precipitation intensity due to aerosol perturbation is a robust feature, not contingent on a specific environmental setup.

These supplementary simulations demonstrate that the core findings of this study—namely, the differential impact of urban aerosols and land use on precipitation in both urban and non-urban areas—are not artifacts of a singular event. Instead, they remain valid under a range of plausible atmospheric conditions. Thus, this analysis extends the applicability of our conclusions and strengthens their relevance to broader urban precipitation physics and dynamics.

6. Discussions

6.1. Individual effects of urban aerosols and land use

This study demonstrates that both urban aerosols and land use influence precipitation processes in both the urban and adjacent non-urban areas through distinct mechanisms. Urban aerosols enhance condensation, which intensifies updrafts. This results in increased precipitation frequency and cumulative rainfall in the urban area. However, the stronger convection in the urban area also draws convective energy away from the neighboring non-urban area, thereby suppressing very heavy precipitation there. This indicates a cross-regional teleconnection mediated by mesoscale circulations influenced by spatial aerosol gradients. Conversely, urban land use—represented mainly by the built-up surface—suppresses surface latent-heat fluxes, thereby weakening moist instability and updraft strength. This leads to decreased precipitation within the urban core but the reduced transport of convective energy into the urban core and increased convective energy in the adjacent non-urban area, thereby enhancing precipitation there.

The contrasting mechanisms underline the importance of considering aerosol and land-use effects simultaneously when assessing urban impacts on regional hydrometeorology. Moreover, this study's finding that the spatiotemporal distribution of convective energy is altered between the urban and non-urban areas based on urban aerosol load and surface characteristics illustrates how localized urbanization can disrupt regional energy balances and associated hydrological outcomes across the areas. This underlines the importance of considering both the urban and non-urban areas for the assessment of urban influences.

6.2. Combined effects of urban aerosols and land use

The combined effect of elevated aerosols and urban land use in the urban area results in a net increase in precipitation compared to a scenario with reduced aerosols as in the no_ub_aro run, but a net decrease compared to a scenario with non-urban land use as in the no_ub_sfc run (Fig. 3). The aerosol-induced enhancement of precipitation is partially offset by the suppressive effect of urban land use in the urban area (Fig. 3). Hence, the control run's cumulative precipitation lies between the no_ub_aro and no_ub_sfc runs, indicating that the positive effect of aerosols on precipitation is moderated by the negative effect of urban land use in the urban area. This interplay suggests that aerosols drive stronger convective processes, but urban land use limits the availability of the convective energy, constraining the full potential of aerosol-driven precipitation enhancement in the urban area.

The combined effect of urban aerosols and land use in the urban area leads to a net increase in cumulative precipitation in the non-urban area compared to scenarios where either factor is absent (Fig. 3). Aerosol-induced enhancement of precipitation is further enhanced by impacts of urban land use on precipitation (Fig. 3), hence, impacts of aerosols on precipitation and those of urban land use are additive to each other, although urban aerosols reduce heavy precipitation in the non-urban area.

7. Summary and conclusions

Our CSRM-based analysis of individual effects of urban aerosols and land use on an MCS event over the Seoul region shows that:

- Urban aerosol loading increases moderate, heavy and very heavy precipitation in the urban area but reduces very heavy precipitation in the nearby non-urban area via processes involving aerosol-induced condensation and altered MSE fluxes.
- Urban land use suppresses urban moderate, heavy and very heavy precipitation by weakening urban moist instability but enhances light, moderate, heavy and very heavy precipitation in the adjacent non-urban area by redistributing the MSE.
- The spatial inhomogeneity of aerosol and land surface conditions between the urban and non-urban areas creates teleconnections that control mesoscale precipitation distributions.

These results highlight that impacts of urbanization on precipitation extend beyond city boundaries and are tele-connected to precipitation in the adjacent non-urban area. Moreover, the ways in which these impacts propagate differ between urban aerosols and urban land use. This underscores the need to evaluate urbanization effects within an integrated urban–non-urban framework—one that jointly considers aerosol loading and land-use change—to achieve a more complete understanding of how cities reshape regional precipitation patterns.

The discussed combined effects of urban aerosols and land use suggest that urban planning must account for both aerosol emissions and land use changes to manage precipitation patterns effectively. Strategies to mitigate urban heat island effects (e.g., increasing green spaces to enhance latent-heat fluxes) could amplify aerosol-driven precipitation increases in urban areas but may dampen aerosol-driven precipitation increases in adjacent non-urban areas. Reducing aerosol emissions might decrease urban precipitation but increase very heavy precipitation in non-urban areas. These findings emphasize the importance of integrated approaches to urban development that consider regional hydrometeorological impacts.

Looking ahead, there remains a need to extend the results beyond the single case study by utilizing long-term ground and satellite observation data which span over tens of years. Future studies, utilizing these long-term observational data, should analyze the statistical patterns of aerosol and land-use impacts on precipitation under varying urban, climate conditions, with a particular focus on extreme weather events and seasonal and yearly variations. Moreover, exploring ways to link hydrometeorological outcomes with urban policy and planning, especially in terms of flood risk and water resource management, will be crucial. Regarding this, future research should develop and apply metrics that quantify societal relevance, such as population-weighted precipitation anomalies or risk exposure indices, to assess how urban-induced precipitation changes translate into human impacts. This direction will advance both the scientific understanding and the practical management of urbanization-driven changes in regional precipitation systems.

CRediT authorship contribution statement

Seoung Soo Lee: Supervision, Methodology, Investigation, Conceptualization, Writing – original draft. **Jinho Choi:** Validation, Software, Formal analysis, Data curation. **Hyunkyoung Kim:** Visualization. **Sang-Keun Song:** Funding acquisition, Writing – review & editing. **Junshik Um:** Investigation, Writing – review & editing. **Kyong-Hwan Seo:** Writing – review & editing. **Chang Hoon Jung:** Writing – review & editing. **Manguttathil G. Manoj:** Writing – review & editing.

Declaration of competing interest

The authors declare that they have no known competing financial interests or personal relationships that could have appeared to influence the work reported in this paper.

Acknowledgements

This study is supported by the National Research Foundation of Korea (NRF) grant funded by the Korea government (MSIT) (Nos. NRF2023R1A2C1002367 and RS-2025-00572970), and the Korea Meteorological Administration Research and Development Program “Research on Weather Modification and Cloud Physics” under Grant (KMA2018-00224), and Korea Institute of Marine Science and Technology Promotion (KIMST) funded by the Ministry of Oceans and Fisheries, Korea (RS-2021-KS211502). This study is supported by Global Learning and Academic research institution for Master’s·PhD students, and Postdocs (LAMP) Program of the National Research Foundation of Korea (NRF) grant funded by the Ministry of Education (No. RS-2023-00301938) and by Basic Science Research Program through the National Research Foundation of Korea (NRF) funded by the Ministry of Education (RS-2020-NR049592).

Data availability

Our private computer system stores private data such as the model code and output, and the observation data. Upon approval from funding sources, the data will be opened to the public. Projects related to this paper have not been finished, thus, the sources prevent the data from being open to the public currently. However, if information on the data is needed, contact the corresponding author Seoung Soo Lee (slee1247@umd.edu).

References

Baik, J.-J., Kim, Y.-H., Chun, H.-Y., 2001. Dry and moist convection forced by an urban heat island. J. Appl. Meteorol. 40, 1462–1475.

Bell, T.L., Rosenfeld, D., Kim, K.M., et al., 2008. Midweek increase in U.S. summer rain and storm heights suggests air pollution invigorates rainstorms. J. Geophys. Res. 113. https://doi.org/10.1029/2007JD008623. D02209.
Bercos-Hickey, E., Nathan, T., Chen, S.-H., 2017. Saharan dust and the African easterly jet – African easterly wave system: structure, location and energetics. Q. J. R. Meteorol. Soc. 143, 2797–2808.
Bouvette, T., Lambert, J.L., Bedient, P.B., 1982. Revised rainfall frequency analysis for Houston. J. Hydraul. Div. Proc. Amer. Soc. Civil. Eng. 108, 515–528.
Brown, A., Milton, S., Cullen, M., Golding, B., Mitchell, J., Shelly, A., 2012. Unified modeling and prediction of weather and climate: a 25-year journey. Bull. Am. Meteorol. Soc. 93, 1865–1877.
Burian, S.J., Shepherd, J.M., 2005. Effects of urbanization on the diurnal rainfall pattern in Houston: hydrological processes. Rainfall Hydrol. Proc. 19, 1089–1103.
Casquero-Vera, J.A., Lyamani, H., Titos, G., Moreira, G. de A., Benavent-Oltra, J.A., Conte, M., Contini, D., Järvi, L., Olmo-Reyes, F.J., Alados-Arboledas, L., 2022. Aerosol number fluxes and concentrations over a southern European urban area. Atmos. Environ. 269, 118849. https://doi.org/10.1016/j.atmosenv.2021.118849.
Chen, F., Dudhia, J., 2001. Coupling an advanced land-surface hydrology model with the Penn State-NCAR MM5 modeling system. Part I: model description and implementation. Mon. Weather Rev. 129, 569–585.
Chen, S., et al., 2015. Urbanization effect on precipitation over the Pearl River Delta based on CMORPH data. Adv. Clim. Chang. Res. 6, 16–22.
Climate Change Science Program and Subcommittee on Global Change Research, 2003. Strategic plan for the U.S. Climate Change Science Program. Final Rep. 221 available online at http://climatescience.gov.
Diem, J.E., Brown, D.P., 2003. Anthropogenic impacts on summer precipitation in Central Arizona, U. S. A. Prof. Geogr. 55, 343–355.
Fan, J., Yuan, T., Comstock, J.M., et al., 2009. Dominant role by vertical wind shear in regulating aerosol effects on deep convective clouds. J. Geophys. Res. 114. https://doi.org/10.1029/2009JD012352.
Fan, J., Zhang, Y., Li, Z., Hu, J., Rosenfeld, D., 2020. Urbanization-induced land and aerosol impacts on sea-breeze circulation and convective precipitation. Atmos. Chem. Phys. 20, 14163–14182. https://doi.org/10.5194/acp-20-14163-2020.
Fouquart, Y., Bonnel, B., 1980. Computation of solar heating of the earth's atmosphere: a new parameterization. Beitr. Phys. Atmos. 53, 35–62.
Haberlie, A.M., Ashley, W.S., Pingel, T.J., 2015. The effect of urbanization on the climatology of thunderstorm initiation. Q. J. R. Meteorol. Soc. 141, 663–675.
Hidaldo, J., Masson, V., Gimeno, L., 2010. Scaling the daytime urban heat island and urban-breeze circulation. J. Appl. Meteorol. Climatol. 49, 889–901.
Holben, B.N., Tanre, D., Smirnov, A., et al., 2001. An emerging ground-based aerosol climatology: aerosol optical depth from AERONET. J. Geophys. Res. 106, 12,067–12,097.
Khain, A., Pokrovsky, A., Rosenfeld, D., Blahak, U., Ryzhkoy, A., 2011. The role of CCN in precipitation and hail in a mid-latitude storm as seen in simulations using a spectral (bin) microphysics model in a 2D dynamic frame. Atmos. Res. 99, 129–146.
King, J., 2009. Automatic Weather Stations. available at https://web.archive.org/web/20090522121225/http://www.automaticweatherstation.com/index.html.
Koop, T., Luo, B.P., Tsias, A., Peter, T., 2000. Water activity as the determinant for homogeneous ice nucleation in aqueous solutions. Nature 406, 611–614.
Korean Meteorological Administration, 2025. Precipitation Classification. available at https://www.weather.go.kr/w/community/knowledge/fct-term-exp.do.
Lau, K.M., Kim, M.-K., 2006. Observational relationships between aerosol and Asian monsoon rainfall, and circulation. Geophys. Res. Lett. 33, L21810. https://doi.org/10.1029/2006GL027546.
Lebo, Z.J., Morrison, H., 2014. Dynamical effects of aerosol perturbations on simulated idealized squall lines. Mon. Weather Rev. 142, 991–1009.
Lee, S.S., 2012. Effect of aerosol on circulations and precipitation in deep convective clouds. J. Atmos. Sci. 69, 1957–1974.
Lee, S.S., Donner, L.J., Phillips, V.T.J., Ming, Y., 2008. The dependence of aerosol effects on clouds and precipitation on cloud-system organization, shear and stability. J. Geophys. Res. 113, D16202. https://doi.org/10.1029/2007JD009224.
Lee, S.S., Feingold, G., Koren, I., Yu, H., et al., 2014. Effect of gradients in biomass burning aerosol on circulations and clouds. J. Geophys. Res. 119, 9948–9964.
Lee, S.S., Kim, B.-G., Yum, S.S., et al., 2016. Effect of aerosol on evaporation, freezing and precipitation in a multiple cloud system. Clim. Dyn. 48, 1069–1087.
Lee, S.S., Kim, B.-G., Li, Z., Choi, Y.-S., Jung, C.-H., Um, J., Mok, J., Seo, K.-H., 2018. Aerosol as a potential factor to control the increasing torrential rain events in urban areas over the last decades. Atmos. Chem. Phys. 18, 12,531–12,550.
Leung, G.R., van den Heever, S.C., 2023. Aerosol breezes drive cloud and precipitation increases. Nat. Commun. 14, 2357. https://doi.org/10.1038/s41467-023-37722-3.
Li, M., Wang, T., Xie, M., Zhuang, B., Li, S., Han, Y., Cheng, N., 2017. Modeling of urban heat island and its impacts on thermal circulations in the Beijing–Tianjin–Hebei region, China. Theor. Appl. Climatol. 128, 999–1013.
Li, J., Zhou, W., Tao, C., 2024. The impact of urbanization on surface runoff and flood prevention strategies: a case study of a traditional village. Land 13, 1528. https://doi.org/10.3390/land13091528.
Lin, Y., Fan, J., Jeong, J.-H., Zhang, Y., Homeyer, C.R., Wang, J., 2021. Urbanization-induced land and aerosol impacts on storm propagation and hail characteristics. J. Atmos. Sci. 78, 925–947.
Lohmann, U., Diehl, K., 2006. Sensitivity studies of the importance of dust ice nuclei for the indirect aerosol effect on stratiform mixed-phase clouds. J. Atmos. Sci. 63, 968–982.
Masson, V., Lemonsu, A., Hidalgo, J., Voogt, J., 2020. Urban climates and climate change. Annu. Rev. Environ. Resour. 45, 411–444.
McLeod, J., Shepherd, M., Konrad, C.E., 2017. Spatio-temporal rainfall patterns around Atlanta, Georgia and possible relationships to urban land cover. Urban Clim. 21, 27–42. https://doi.org/10.1016/j.uclim.2017.03.004.
McLeod, J., Shepherd, M., Appelbaum, M., 2024. Evidence of cloud and rainfall modification in a mid-sized urban area – A climatological analysis of Augusta, Georgia. City Environ. Interact. 21, 100141. https://doi.org/10.1016/j.cacint.2024.100141.
Menon, S., Hansen, J., Nazarenko, L., Luo, Y., 2002. Climate effects of black carbon aerosols in China and India. Science 297. https://doi.org/10.1126/science.1075159.
Miller, J.D., Hutchins, M., 2017. The impacts of urbanization and climate change on urban flooding and urban water quality: a review of the evidence concerning the United Kingdom. J. Hydrol.: Region. Stud. 12, 345–362.
Mlawer, E.J., Taubman, S.J., Brown, P.D., Iacono, M.J., Clough, S.A., 1997. RRTM, a validated correlated-k model for the longwave. J. Geophys. Res. 102, 16,663–16,682.
Möhler, O., et al., 2006. Efficiency of the deposition mode ice nucleation on mineral dust particles. Atmos. Chem. Phys. 6, 3007–3021.
Morrison, H., Grabowski, W.W., 2011. Cloud-system resolving model simulations of aerosol indirect effects on tropical deep convection and its thermodynamic environment. Atmos. Chem. Phys. 11, 10,503–10,523.
Niyogi, D., Pyle, P., Lei, M., Arya, S.P., Kishtawal, C.M., Shepherd, J.M., Chen, F., Wolfe, B., 2011. Urban modification of thunderstorms: an observational storm climatology and model case study for the Indianapolis urban region. J. Appl. Meteorol. Climatol. 50, 1129–1144. https://doi.org/10.1175/2010JAMC1836.1.
Pruppacher, H.R., Klett, J.D., 1978. Microphysics of Clouds and Precipitation. D. Reidel, p. 714.
Reale, O., Lau, K.M., Silva, A., 2011. Impact of interactive aerosol on the African easterly jet in the NASA GEOS-5 global forecasting system, Wea. Forecasting 26, 504–519.
Rotstayn, L.D., Lohmann, U., 2002. Tropical rainfall trends and the indirect aerosol effect. J. Clim. 15, 2103–2016.
Rotstayn, L.D., et al., 2007. Have Australian rainfall and cloudiness increased due to the remote effects of Asian anthropogenic aerosols? J. Geophys. Res. 112, D09202.
Sato, T., Hino, H., Kusaka, H., 2020. Separating urban heat island circulation and convective cells through dynamic mode decomposition. Atmos. Sci. Lett. 21, e1279. https://doi.org/10.1002/asl.1279.
Shelley, A., Mao, A., Blanco, A., et al., 2014. Houston-Galveston-Brazoria (HGB) PM2.5 Advance Path Forward. draft obtainable from. https://www.epa.gov/sites/production/files/2016-02/documents/20140717houstonpath.pdf.
Shepherd, J.M., 2005. A review of current investigations of urban-induced rainfall and recommendations for the future. Earth Interact. 9, 1–27.

Shepherd, J.M., Pierce, H., Negri, A.J., 2002. Rainfall modification by major urban areas: observations from spaceborne rain radar on the TRMM satellite. J. Appl. Meteorol. 41, 689–701.

Skamarock, W.C., Klemp, J.B., Dudhia, J., Gill, D.O., Barker, D.M., Duda, M.G., Huang, X.-Y., Wang, W., Powers, J.G., 2008. A Description of the Advanced Research WRF Version 3 (NCAR Technical Note NCAR/TN-475+STR). National Center for Atmospheric Research. https://doi.org/10.5065/D68S4MVH.

Sterzinger, L.J., Sedlar, J., Guy, H., Neely III, R.R., Igel, A.L., 2022. Do Arctic mixed-phase clouds sometimes dissipate due to insufficient aerosol? Evidence from comparisons between observations and idealized simulations. Atmos. Chem. Phys. 22, 8973–8988.

van den Heever, S.C., Cotton, W.R., 2007. Urban aerosol impacts on downwind convective storms. J. Appl. Meteorol. Climatol. 46, 828–850. https://doi.org/10.1175/JAM2492.1.

Wang, H., Feingold, G., 2009. Modeling mesoscale cellular structures and drizzle in marine stratocumulus. Part I: impact of drizzle on the formation and evolution of open cells. J. Atmos. Sci. 66, 3237–3256.

Wang, X., Kinsland, G., Poudel, D., Fenech, A., 2019. Urban flood prediction under heavy precipitation. J. Hydrol. https://doi.org/10.1016/j.jhydrol.2019.123984.

Weisman, M.L., Klemp, J.B., 1982. The dependence of numerically simulated convective storms on vertical wind shear and buoyancy. Mon. Weather Rev. 110, 504–520.

Wilcox, E.K., Lau, K.-M., Kim, K.M., 2010. A northward shift of the North Atlantic Ocean intertropical convergence zone in response to summertime Saharan dust outbreaks. Geophys. Res. Lett. 37, L04804. https://doi.org/10.1029/2009GL041774.